IJMSO

International Journal of Mathematical Sciences and Optimization: Theory and Applications
12(1), 2026, Pages 104 - 128
https://doi.org/10.5281/zenodo.20467246

Combined Effects of Anisotropic Permeability, Chemical Reaction, and Dual Stratifications on Unsteady Free Convection Around a Vertical Circular Cylinder

A. Adeniyan[1*], Q. O. Rauf[2], A. T. Tiamiyu [3]

1. Mathematics/Statistics Unit, Trinity University, Yaba Lagos, Nigeria.
2. Department of Mathematics, University of Lagos, Akoka, Nigeria.
3. School of Mathematics, Jilin University, Changchun 130012, China.
Email: [1]tunjadeniyan@yahoo.com, [2]qorauf@gmail.com, [3]tiamiyuabdgafar@jlu.edu.cn
* Corresponding author: tunjadeniyan@yahoo.com

Article Info
Received: 25 February 2026 Revised: 22 March 2026
Accepted: 25 March 2026 Available online: 15 April 2026

Abstract

The unsteady free convection boundary layer flow past a vertically translating circular cylinder embedded in a saturated anisotropic porous medium is investigated under simultaneous thermal and solutal stratifications with a first-order homogeneous chemical reaction. The porous resistance is modelled with a tensor-based Darcy–Brinkman formulation in which the permeability is represented by a symmetric positive-definite second-order tensor, and wall suction/injection is permitted. Using boundary-layer scaling and similarity transformations, the governing PDE system is reduced to a seventh-order nonlinear two-point boundary value problem. The reduced system is solved by an adaptive Lobatto IIIa collocation scheme, selected for its A-stability and reliable performance on stiff boundary-layer equations. The solver reproduces the Crane flat-plate exact solution to six decimal places and matches published stretching-cylinder data to within 2%. The results show that porous drag and transverse curvature govern wall shear and heat transfer, the Schmidt number and chemical reaction strength govern mass transfer, and thermal stratification enhances the Nusselt number through boundary layer thinning. Global sensitivity analysis using Latin Hypercube sampling identifies the Prandtl number as most influential for heat transfer, the Schmidt number for mass transfer, and the porous drag parameter for skin friction. The main contribution is the unified treatment of anisotropic tensor permeability, chemical reaction, and dual stratification for an unsteady translating cylinder, together with quantitative ranking of parameter influence under a single consistent modelling framework. The results are relevant to geothermal energy extraction, contaminant transport in stratified aquifers, and catalytic processes in enhanced oil recovery.

Keywords: Chemical reaction, Anisotropic porous medium, Free convection, Circular cylinder, Dual stratification.
MSC2010: 35Q20.

IJMSO

International Journal of Mathematical Sciences and Optimization: Theory and Applications
12(1), 2026, Pages 104 - 128
https://doi.org/10.5281/zenodo.20467246

1 Introduction

Unsteady laminar free convection flow past a circular cylinder arises in a variety of engineering and geophysical contexts, including nuclear reactor cooling, geothermal energy extraction, catalytic processes in crude oil recovery, and contaminant migration in underground aquifers. Although natural convection over cylindrical geometries has been extensively studied, the simultaneous interaction of anisotropic porous permeability, first-order chemical reactions, and dual thermal-solutal stratifications in an unsteady framework for a moving cylinder remains largely unexplored in the literature. The present work addresses this gap.

Anisotropic porous media appear naturally in geological formations where layered soils, sedimentary rock strata, and fibrous composites exhibit direction-dependent permeability. The permeability of such a medium is characterized by a symmetric positive-definite second-order tensor $\bar{\bar{K}} \in \mathbb{R}^{2\times 2}_{\text{sym}}$ whose eigenvalues and eigenvectors govern the directional resistance to flow. Degan et al. [1] analysed convective heat transfer in a vertical anisotropic porous layer, and the same group later examined similarity regimes in cylindrical geometries [2]. Vajravelu and Prasad [3] studied mixed convection in an anisotropic porous layer with oblique principal axes. Nakayama et al. [4] and Roper et al. [5] investigated flow through anisotropic rod arrays and microlattice structures, respectively. The effects of rotation and radiation on convection in anisotropic porous media were examined by Slimi et al. [6] and Bhadauria et al. [7]. More recent contributions include the smoothed particle hydrodynamics study of Aly and Ahmed [8] for non-Darcy anisotropic media and the correlations of Iasiello et al. [9] for open-cell metal foams. Ali et al. [10] examined double-diffusive convection in an anisotropic porous layer under rotational modulation, and Garg et al. [11] analysed triply diffusive thermo-bio-convection in an anisotropic porous medium with internal heating. Keshavarzian and Sayehvand [12] recently assessed the validity of the boundary layer approximation for natural convection around cylinders in porous media. The monograph of Nield and Bejan [13] provides a theoretical treatment.

In many environmental and engineering settings, the ambient fluid exhibits non-uniform temperature or concentration distributions. Cheng [14,15] conducted systematic studies of double-diffusive natural convection along vertical wavy surfaces in stratified porous media. Earlier similarity analyses for thermally stratified environments were developed by Kulkarni et al. [16] and Angirasa and Srinivasan [17]. For cylindrical geometries, Deka and Paul [18] treated flow past infinite vertical cylinders with dual stratification, and Jha and Musa [19] examined the combined effects of anisotropy and stable stratification in vertical annuli; this was later extended by the same group to asymmetric heating [20] and buoyancy-driven Couette flow [21] in anisotropic porous channels. Adigun et al. [22] investigated dual stratification with MHD slip-flow over a stretched inclined cylinder in a porous medium. Thebault et al. [23] and Srinivasacharya and RamReddy [24] explored stratification effects in finite channels and non-Darcy micropolar fluids, respectively.

First-order chemical reactions within the concentration boundary layer consume or generate solute, steepening the near-wall concentration gradient and modifying its coupling to the velocity and thermal fields. Mansour et al. [25] and Kandasamy et al. [26] analysed first-order chemical reactions combined with thermal stratification in MHD free convective flows. Ibrahim et al. [27] studied radiation and chemical reaction effects on unsteady MHD free convection past a permeable plate. Chamkha et al. [28] investigated chemical reaction effects on natural convection in porous media, while Mahdy [29] considered variable-viscosity double-diffusive convection with chemical reaction. Sudarsana Reddy and Sreedevi [30] and Zhang et al. [31] examined the combined effects of radiation and chemical reactions on nanofluid flows. Singh and Chauhan [32] recently studied chemical reaction effects on nanofluid flow from a permeable stretching cylinder in a porous medium with convective boundary conditions. Badday and Harfash [33] analysed double-diffusive convection with chemical reaction and magnetic field effects in bidispersive porous media, and Zegeye et al. [34] studied the combined non-linear effects of Joule heating and binary chemical reaction past an unsteady stretching cylinder in a Darcy–Forchheimer porous medium. Isede et al. [35] conducted an analytical study on entropy optimization and heat transfer of MHD heat-generating flows through anisotropic porous media. Gbadeyan et al. [36] examined the influence of Dufour and Soret effects on

IJMSO

International Journal of Mathematical Sciences and Optimization: Theory and Applications
12(1), 2026, Pages 104 - 128
https://doi.org/10.5281/zenodo.20467246

unsteady MHD convective heat and mass transfer in a non-Darcy porous medium. Nguyen et al. [37] studied unsteady reaction-driven flow from anisotropic cylinders, and Rashad [38] investigated anisotropic slip effects on unsteady nanofluid flows over inclined surfaces.

Despite the extensive body of work reviewed above, very few studies have treated anisotropic porous permeability, homogeneous chemical reaction, dual thermal–solutal stratification, and unsteady cylinder translation within one unified boundary-layer framework. In particular, the present model combines tensor-based permeability representation with global sensitivity quantification in the same formulation. The similarity reduction approach adopted here builds upon the work of Crane [39] on stretching sheets, extended to cylindrical geometry by Wang [40]. Recent Darcy–Brinkman studies of stretching cylinder flows include Znaidia et al. [41], who employed a Brinkman–Maxwell–Garnett model for drilling nanofluids. Benchmark heat transfer results for stretching cylinders were established by Ishak et al. [42], Bachok and Ishak [43], and Elbashbeshy [44], while related double-diffusive studies on vertical cylinders include Chen and Yuh [45] and Khan et al. [46].

The novelty of the present study is the unified formulation and analysis of these four coupled effects for a vertically translating circular cylinder in an anisotropic porous medium, together with a similarity reduction to a seventh-order boundary value problem and a benchmarked parametric and sensitivity study of the resulting transport behaviour.

The remainder of the manuscript is organised as follows. Section 2 presents the mathematical model, governing equations, similarity transformation, and the associated dimensionless parameters and transfer metrics. Section 3 describes the numerical method and verification procedure. Section 4 discusses the parametric and sensitivity results. Finally, Section 5 summarises the main findings, practical implications, and limitations of the study.

2 Mathematical formulation

2.1 Problem statement and governing assumptions

Consider the unsteady, two-dimensional, laminar free convection boundary layer flow of an incompressible fluid past a semi-infinite vertical circular cylinder of radius a. The cylinder translates axially with prescribed velocity $U_w(z,t)$ and is embedded in a saturated anisotropic porous medium. The medium is characterised by principal permeabilities k_1 and k_2, with the k_1-axis inclined at angle θ^* to the cylinder axis. A cylindrical coordinate system (z,r) is adopted, with z along the vertical axis and r the radial distance from the axis of symmetry.

The following assumptions are adopted throughout. The Boussinesq approximation holds, so $\rho = \rho_\infty[1-\beta(T-T_\infty)-\beta^*(C-C_\infty)]$, valid for $|\Delta T|/T_\infty \ll 1$. The porous resistance follows the Darcy–Brinkman formulation with anisotropic permeability tensor $\bar{\bar{K}}$. A first-order homogeneous chemical reaction of rate constant K_r acts on the excess concentration $(C-C_\infty)$. The ambient temperature and concentration vary linearly with height, characterised by stratification parameters S_1 and S_2, respectively. Wall suction or injection is imposed through a prescribed radial velocity V_w at the cylinder surface.

The physical configuration and coordinate system are depicted in Figure 1. As illustrated, a vertical circular cylinder of radius a translates upward with velocity U_w through a saturated anisotropic porous medium whose permeability tensor $\bar{\bar{K}} = \boldsymbol{R}\,\mathrm{diag}(k_1,k_2)\,\boldsymbol{R}^\top$ has its k_1-axis inclined at angle θ^* to the cylinder axis. The cylinder motion is aligned with the gravitational body force in the aiding buoyancy configuration, so that both thermal and solutal buoyancy forces assist the flow along the positive z-direction. Velocity, thermal, and solutal boundary layers develop simultaneously along the curved surface. The ambient temperature and concentration vary linearly with height as $T_\infty(z)$ and $C_\infty(z)$, respectively, while a first-order chemical reaction of rate constant K_r acts on the excess concentration within the boundary layer. Wall suction or injection is permitted through a prescribed radial velocity V_w at the cylinder surface.

IJMSO
International Journal of Mathematical Sciences and Optimization: Theory and Applications
12(1), 2026, Pages 104 - 128
https://doi.org/10.5281/zenodo.20467246

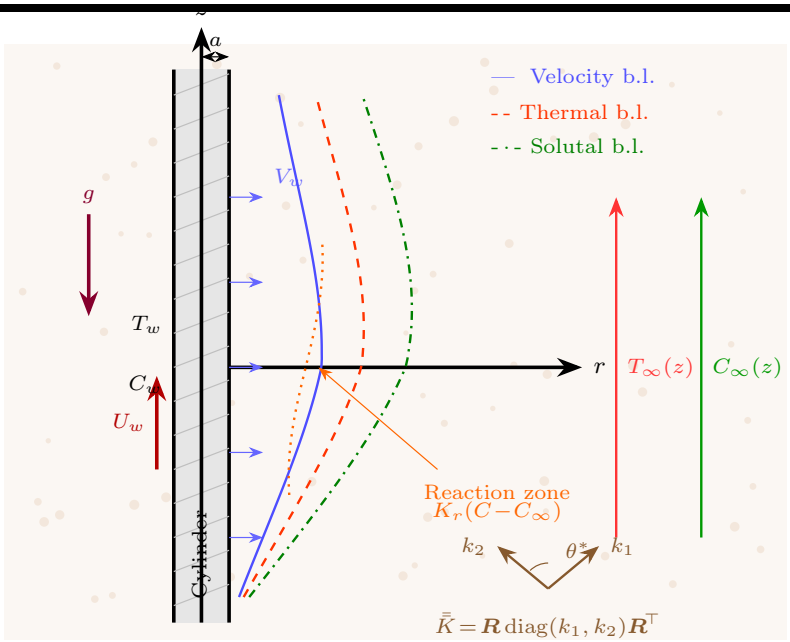

Figure 1: Schematic of the physical configuration and coordinate system.

2.2 Governing equations and porous medium model

Under the above assumptions, the conservation equations for mass, momentum, energy, and species concentration take the form:

$$\nabla \cdot \boldsymbol{v} = 0, \tag{2.1}$$

$$\frac{\partial \boldsymbol{v}}{\partial t} + (\boldsymbol{v} \cdot \nabla)\,\boldsymbol{v} = \nu_{\text{eff}}\,\nabla^2 \boldsymbol{v} + g\big[\beta(T - T_\infty) + \beta^*(C - C_\infty)\big]\,\hat{\boldsymbol{e}}_z - \nu\,\bar{\bar{K}}^{-1}\,\boldsymbol{v}, \tag{2.2}$$

$$\frac{\partial T}{\partial t} + \boldsymbol{v} \cdot \nabla T = \alpha\,\nabla^2 T, \tag{2.3}$$

$$\frac{\partial C}{\partial t} + \boldsymbol{v} \cdot \nabla C = D_m\,\nabla^2 C - K_r\,(C - C_\infty), \tag{2.4}$$

where $\boldsymbol{v} = (u, v)$ is the velocity vector with u and v the axial and radial velocity components, respectively, $\hat{\boldsymbol{e}}_z$ is the unit vector along the cylinder axis, and $-K_r(C - C_\infty)$ models the first-order homogeneous reaction. Stratification enters through the ambient gradients: decomposing $T = T_\infty(z) + \Delta T$ and $C = C_\infty(z) + (C - C_\infty)$ introduces advection terms $u\,(\mathrm{d}T_\infty/\mathrm{d}z) = S_1\,u$ and $u\,(\mathrm{d}C_\infty/\mathrm{d}z) = S_2\,u$, as shown in the boundary layer equations Equations (2.19) and (2.20).

The symmetric positive-definite permeability tensor for an anisotropic porous medium with principal permeabilities k_1 and k_2, with the k_1-principal axis inclined at angle θ^* to the z-axis, is obtained by a standard rotation of the diagonal representation $\mathrm{diag}(k_1, k_2)$ [1, 13]:

$$\bar{\bar{K}} = \boldsymbol{R}(\theta^*)\;\mathrm{diag}(k_1, k_2)\,\boldsymbol{R}^\top(\theta^*) = \begin{pmatrix} K_{11} & K_{12} \\ K_{12} & K_{22} \end{pmatrix}, \tag{2.5}$$

where $\boldsymbol{R}(\theta^*)$ is the planar rotation matrix and

$$K_{11} = k_1 \cos^2\theta^* + k_2 \sin^2\theta^*, \tag{2.6}$$

$$K_{22} = k_1 \sin^2\theta^* + k_2 \cos^2\theta^*, \tag{2.7}$$

$$K_{12} = (k_1 - k_2)\sin\theta^* \cos\theta^*. \tag{2.8}$$

IJMSO
International Journal of Mathematical Sciences and Optimization: Theory and Applications
12(1), 2026, Pages 104 - 128
https://doi.org/10.5281/zenodo.20467246

The off-diagonal elements involve the factor $(k_1 - k_2)$, which follows directly from the similarity transformation of a diagonal matrix. In the isotropic limit $k_1 = k_2$, the off-diagonal entries vanish identically, as required by physical consistency.

Defining the permeability ratio $k^* := k_1/k_2$, the effective directional permeability parameter that arises upon projecting the Darcy resistance along the axial direction within the boundary layer approximation is

$$K_a := k^* \sin^2\theta^* + \cos^2\theta^*. \tag{2.9}$$

One verifies that $K_a = 1$ when $k^* = 1$ (isotropic limit, for any θ^*) or when $\theta^* = 0$ (the k_1-axis aligned with the flow direction, for any k^*). When $\theta^* = \pi/2$, $K_a = k^*$ and the axial flow resistance is governed entirely by k_2.

2.3 Initial and boundary conditions, stratification, and boundary layer equations

$$t \le 0: \quad u = 0, \quad T = T_\infty, \quad C = C_\infty \qquad \text{for all } r, \tag{2.10}$$

$$t > 0: \quad u = U_w, \quad v = V_w, \quad -k\left.\frac{\partial T}{\partial r}\right|_{r=a} = q_w, \quad C = C_w \qquad \text{at } r = a, \tag{2.11}$$

$$u \to 0, \quad T \to T_\infty, \quad C \to C_\infty \qquad \text{as } r \to \infty. \tag{2.12}$$

Following Jha and Musa [19], the thermal stratification parameter is defined as

$$S_1 = \frac{\mathrm{d}T_\infty}{\mathrm{d}z} + \frac{g}{C_p}, \tag{2.13}$$

where $\mathrm{d}T_\infty/\mathrm{d}z$ is the vertical temperature lapse rate and $g/C_p \approx 10\,^\circ\mathrm{C\,km^{-1}}$ is the dry adiabatic lapse rate. The atmosphere is stably stratified when $S_1 > 0$, neutrally stratified when $S_1 = 0$, and unstably stratified when $S_1 < 0$. The solutal stratification parameter is defined analogously:

$$S_2 = \frac{\mathrm{d}C_\infty}{\mathrm{d}z}. \tag{2.14}$$

Following Bachok and Ishak [43], Elbashbeshy [44], and Adigun et al. [22], the temperature and concentration differences are expressed as

$$T - T_\infty = \frac{q_w}{k}\sqrt{\frac{\nu z}{U_w}}\,\theta(\eta), \qquad q_w = \frac{q_{w0}}{l\,(1-\lambda t)}\,z^n, \tag{2.15}$$

$$C - C_\infty = (C_w - C_\infty)\,\phi(\eta). \tag{2.16}$$

Applying the standard boundary layer scalings ($v \ll u$, $\partial/\partial z \ll \partial/\partial r$) to Equations (2.1) to (2.4) yields, in cylindrical coordinates (z, r):

$$\frac{\partial(u\,r)}{\partial z} + \frac{\partial(v\,r)}{\partial r} = 0, \tag{2.17}$$

$$\frac{\partial u}{\partial t} + u\,\frac{\partial u}{\partial z} + v\,\frac{\partial u}{\partial r} = \nu_{\text{eff}}\left(\frac{\partial^2 u}{\partial r^2} + \frac{1}{r}\,\frac{\partial u}{\partial r}\right) + g\big[\beta(T - T_\infty) + \beta^*(C - C_\infty)\big] - \frac{K_a\,\nu}{k_1}\,u, \tag{2.18}$$

$$\frac{\partial T}{\partial t} + u\,\frac{\partial T}{\partial z} + v\,\frac{\partial T}{\partial r} = \alpha\left(\frac{\partial^2 T}{\partial r^2} + \frac{1}{r}\,\frac{\partial T}{\partial r}\right) - S_1\,u, \tag{2.19}$$

$$\frac{\partial C}{\partial t} + u\,\frac{\partial C}{\partial z} + v\,\frac{\partial C}{\partial r} = D_m\left(\frac{\partial^2 C}{\partial r^2} + \frac{1}{r}\,\frac{\partial C}{\partial r}\right) - K_r(C - C_\infty) - S_2\,u. \tag{2.20}$$

IJMSO

International Journal of Mathematical Sciences and Optimization: Theory and Applications
12(1), 2026, Pages 104 - 128
https://doi.org/10.5281/zenodo.20467246

2.4 Similarity transformation

We introduce the similarity variable and stream function following Bachok and Ishak [43]:

$$\eta = \frac{r^2 - a^2}{2a}\sqrt{\frac{U_w}{\nu z}}, \qquad \psi = a\sqrt{\nu\, U_w\, z}\, f(\eta), \tag{2.21}$$

together with the dimensionless temperature and concentration:

$$\theta(\eta) = \frac{k}{q_w}\sqrt{\frac{U_w}{\nu z}}\,(T - T_\infty), \qquad \phi(\eta) = \frac{C - C_\infty}{C_w - C_\infty}, \tag{2.22}$$

where the axial surface velocity is

$$U_w(z,t) = \frac{b\,z}{1-\lambda t}, \qquad b = \frac{U}{l}. \tag{2.23}$$

The stream function satisfies

$$u = \frac{1}{r}\frac{\partial \psi}{\partial r}, \qquad v = -\frac{1}{r}\frac{\partial \psi}{\partial z}, \tag{2.24}$$

so that the continuity equation (2.17) is satisfied identically.

For clarity, the similarity reduction is based on three standard assumptions. First, the boundary-layer ordering $v \ll u$ and $\partial/\partial z \ll \partial/\partial r$ is applied, so axial viscous diffusion and higher-order streamwise derivatives are neglected relative to radial diffusion. Second, pressure-gradient terms are omitted in the transformed momentum equation because the flow is buoyancy-driven with prescribed wall motion in the boundary-layer limit. Third, all dependent variables are scaled with the wall velocity and imposed thermal/solutal driving scales in Equations (2.21) and (2.22), which yields the dimensionless groups in Equations (2.35) to (2.39).

We now outline the key steps of the transformation. From Equations (2.21) and (2.24), the velocity components become

$$u = U_w\, f'(\eta), \qquad v = -\frac{a}{r}\sqrt{\frac{\nu\, U_w}{z}}\, f(\eta). \tag{2.25}$$

Noting from Equation (2.21) that

$$\frac{\partial \eta}{\partial r} = \frac{r}{a}\sqrt{\frac{U_w}{\nu z}}, \qquad \frac{\partial \eta}{\partial t} = \frac{\lambda}{2(1-\lambda t)}\,\eta, \qquad 1 + 2\gamma\eta = \frac{r^2}{a^2}, \tag{2.26}$$

the chain rule gives $\partial/\partial r = (r\sigma/a)\,\mathrm{d}/\mathrm{d}\eta$, where $\sigma := \sqrt{U_w/(\nu z)}$. Applying this to the cylindrical diffusion operator in Equation (2.18) yields

$$\nu_{\text{eff}}\left(\frac{\partial^2 u}{\partial r^2} + \frac{1}{r}\frac{\partial u}{\partial r}\right) = \bar{\gamma}\,\frac{U_w^2}{z}\left[(1+2\gamma\eta)\, f''' + 2\gamma\, f''\right], \tag{2.27}$$

where the $(1 + 2\gamma\eta)$ factor arises from $(r/a)^2 = 1 + 2\gamma\eta$ and the 2γ term from the cylindrical curvature contribution $(1/r)\,\partial u/\partial r$.

The temporal, convective, buoyancy, and Darcy resistance terms transform as

$$\frac{\partial u}{\partial t} = A\,\frac{U_w^2}{z}\left(f' + \tfrac{1}{2}\,\eta\, f''\right), \qquad u\,\frac{\partial u}{\partial z} = \frac{U_w^2}{z}(f')^2, \qquad v\,\frac{\partial u}{\partial r} = -\frac{U_w^2}{z}\, f\, f'', \tag{2.28}$$

$$g\left[\beta(T - T_\infty) + \beta^*(C - C_\infty)\right] = \frac{U_w^2}{z}\,\lambda_T(\theta + Nr\,\phi), \qquad \frac{K_a\,\nu}{k_1}\,u = \frac{U_w^2}{z}\,K_a\,Da\,f'. \tag{2.29}$$

Substituting Equation (2.27)–Equation (2.29) into Equation (2.18) and dividing throughout by U_w^2/z yields the momentum ODE Equation (2.30) below. The energy and species equations Equations (2.31) and (2.32) follow analogously; the $(1 + 2\gamma\eta)$ curvature structure in the diffusion terms and the $A/2$ unsteadiness grouping arise identically in each equation.

IJMSO
International Journal of Mathematical Sciences and Optimization: Theory and Applications
12(1), 2026, Pages 104 - 128
https://doi.org/10.5281/zenodo.20467246

Under the similarity transformation Equation (2.21)–Equation (2.24), the boundary layer problem Equation (2.17)–Equation (2.20) reduces to the following system of coupled nonlinear ordinary differential equations:

$$\bar{\gamma}\big[(1+2\gamma\eta)\,f''' + 2\gamma\,f''\big] + f\,f'' - (f')^2 - A\big(f' + \tfrac{1}{2}\,\eta\,f''\big) + \lambda_T\big(\theta + Nr\,\phi\big) - K_a\,Da\,f' = 0, \tag{2.30}$$

$$\frac{1}{Pr}\big[(1+2\gamma\eta)\,\theta'' + 2\gamma\,\theta'\big] + f\,\theta' - n\,f'\,\theta - \frac{A}{2}\big(\theta + \eta\,\theta'\big) - S\,f' = 0, \tag{2.31}$$

$$\frac{1}{Sc}\big[(1+2\gamma\eta)\,\phi'' + 2\gamma\,\phi'\big] + f\,\phi' - f'\,\phi - \frac{A}{2}\big(\phi + \eta\,\phi'\big) - K\,\phi - F\,f' = 0, \tag{2.32}$$

subject to the boundary conditions

$$f(0) = f_w, \quad f'(0) = 1, \quad \theta'(0) = -1, \quad \phi(0) = 1, \tag{2.33}$$

$$f'(\eta) \to 0, \quad \theta(\eta) \to 0, \quad \phi(\eta) \to 0 \qquad \text{as } \eta \to \infty, \tag{2.34}$$

where $f_w > 0$ corresponds to suction and $f_w < 0$ to injection.

It is worth noting that the unsteady term in Equation (2.32) contains both ϕ and $\eta\,\phi'$, and the convective terms are $f\,\phi' - f'\,\phi$. These arise from the chain rule applied to the material derivative $\mathrm{D}C/\mathrm{D}t$ and must be retained for consistency with the momentum and energy equations.

2.5 Parameters of Engineering Interest

The 14 independent dimensionless parameters appearing in the ODE system Equation (2.30)–Equation (2.32) are defined below. The groups Re_z, Gr_z, Gc_z, and λ_C are intermediate quantities used in the derivation but are absorbed into the independent parameters λ_T, Nr, γ, and Da.

$$A = \frac{\lambda}{b}, \qquad Re_z = \frac{z\,U_w}{\nu}, \qquad Gr_z = \frac{g\,\beta\,q_w\,z^4}{k\,\nu^2}, \qquad Gc_z = \frac{g\,\beta^*(C_w - C_\infty)\,z^3}{\nu^2}, \tag{2.35}$$

$$\lambda_T = \frac{Gr_z}{Re_z^{5/2}}, \qquad \lambda_C = \frac{Gc_z}{Re_z^2}, \qquad Nr = \frac{\lambda_C}{\lambda_T}, \qquad \bar{\gamma} = \frac{\nu_{\text{eff}}}{\nu}, \tag{2.36}$$

$$Pr = \frac{\nu}{\alpha}, \qquad Sc = \frac{\nu}{D_m}, \qquad Da = \frac{\nu\,z}{k_1\,U_w}, \qquad \gamma = \frac{1}{a}\sqrt{\frac{\nu z}{U_w}}, \tag{2.37}$$

$$S = \frac{S_1\,z\,k}{q_w}\sqrt{\frac{U_w}{\nu z}}, \qquad F = \frac{S_2\,z}{C_w - C_\infty}, \qquad K = \frac{K_r\,z}{U_w}, \tag{2.38}$$

$$K_a = k^*\sin^2\theta^* + \cos^2\theta^*, \qquad f_w = -\frac{V_w}{U_w}\sqrt{\frac{z\,U_w}{\nu}}. \tag{2.39}$$

Here A is the unsteadiness parameter, $\bar{\gamma}$ is the viscosity ratio (ν_{eff}/ν), γ is the transverse curvature parameter, λ_T and λ_C are the thermal and solutal buoyancy parameters, Nr is the buoyancy ratio, Da is the porous drag parameter, with larger values indicating stronger flow resistance through the porous matrix, Pr is the Prandtl number, Sc is the Schmidt number, S and F are the thermal and solutal stratification parameters, K_a is the anisotropic permeability parameter, f_w is the suction/injection parameter, and K is the chemical reaction parameter, where $K > 0$ denotes a destructive reaction and $K < 0$ a generative one. The heat flux exponent n characterises the spatial variation of the surface heat flux; the baseline value $n = 1$ corresponds to a linearly varying flux along the cylinder axis, while $n = 0$ yields a uniform flux.

Under the prescribed heat flux condition ($\theta'(0) = -1$), the relevant engineering quantities are:

$$C_f\,Re_z^{1/2} = -f''(0), \qquad Nu_z\,Re_z^{-1/2} = \frac{1}{\theta(0)}, \qquad Sh_z\,Re_z^{-1/2} = -\phi'(0). \tag{2.40}$$

Since the surface heat flux is prescribed, the surface temperature, characterised by $\theta(0)$, is determined as part of the solution. The local Nusselt number is therefore $Nu_z \propto 1/\theta(0)$, rather than the usual $-\theta'(0)$ encountered under prescribed temperature conditions. A smaller $\theta(0)$ indicates enhanced heat transfer.

IJMSO

International Journal of Mathematical Sciences and Optimization: Theory and Applications
12(1), 2026, Pages 104 - 128
https://doi.org/10.5281/zenodo.20467246

3 Numerical method and verification

3.1 Solution procedure

The third-order momentum equation Equation (2.30) and the two second-order equations Equations (2.31) and (2.32), together with seven boundary conditions Equations (2.33) and (2.34), constitute a well-posed two-point boundary value problem (BVP) that we solve on the truncated domain $[0, \eta_{\max}]$.

Setting $\boldsymbol{y} = (y_1, y_2, \ldots, y_7)^\top = (f, f', f'', \theta, \theta', \phi, \phi')^\top$, the system becomes:

$$\boldsymbol{y}' = \boldsymbol{F}(\eta, \boldsymbol{y}; \boldsymbol{p}), \qquad \eta \in [0, \eta_{\max}], \tag{3.1}$$

where $\boldsymbol{p}$ denotes the parameter vector and $\boldsymbol{F}\colon [0, \eta_{\max}] \times \mathbb{R}^7 \to \mathbb{R}^7$ is defined explicitly by

$$y_1' = y_2, \tag{3.2}$$

$$y_2' = y_3, \tag{3.3}$$

$$y_3' = \frac{1}{\bar{\gamma}(1+2\gamma\eta)}\Big[y_2^2 - y_1 y_3 + A\big(y_2 + \tfrac{1}{2}\eta\, y_3\big) - \lambda_T(y_4 + Nr\, y_6) + K_a\, Da\, y_2 - 2\bar{\gamma}\gamma\, y_3\Big], \tag{3.4}$$

$$y_4' = y_5, \tag{3.5}$$

$$y_5' = \frac{Pr}{1+2\gamma\eta}\left[n\, y_2\, y_4 - y_1\, y_5 + \frac{A}{2}(y_4 + \eta\, y_5) + S\, y_2\right] - \frac{2\gamma}{1+2\gamma\eta}\, y_5, \tag{3.6}$$

$$y_6' = y_7, \tag{3.7}$$

$$y_7' = \frac{Sc}{1+2\gamma\eta}\left[y_2\, y_6 - y_1\, y_7 + \frac{A}{2}(y_6 + \eta\, y_7) + K\, y_6 + F\, y_2\right] - \frac{2\gamma}{1+2\gamma\eta}\, y_7. \tag{3.8}$$

The boundary conditions take the separated form:

$$\boldsymbol{g}\big(\boldsymbol{y}(0), \boldsymbol{y}(\eta_{\max})\big) = \boldsymbol{0} \in \mathbb{R}^7. \tag{3.9}$$

The BVP Equation (3.1)–Equation (3.9) is solved using the `scipy.integrate.solve_bvp` routine [47], which implements a collocation method based on the fourth-order Lobatto IIIa formula, a fully implicit, A-stable Runge–Kutta scheme with superconvergent nodal accuracy of order $\mathcal{O}(h^4)$, where h is the local mesh spacing. The solver employs adaptive mesh refinement to satisfy a prescribed relative tolerance of 10^{-8} on the residual.

The far-field boundary is set at $\eta_{\max} = 10$, verified *a posteriori* by confirming that the asymptotic decay conditions $f'(\eta_{\max}), \theta(\eta_{\max}), \phi(\eta_{\max}) < 10^{-6}$ are met. The initial mesh consists of $N = 200$ uniformly spaced nodes. An exponentially decaying initial guess is employed:

$$f^{(0)}(\eta) = f_w + 1 - e^{-\eta}, \quad \theta^{(0)}(\eta) = \tfrac{1}{2}\, e^{-\eta}, \quad \phi^{(0)}(\eta) = e^{-\eta}, \tag{3.10}$$

with derivatives chosen consistently.

In implementation, the profiles in Equation (3.10) are evaluated at the initial mesh nodes and supplied to `solve_bvp` as the initial iterate for the collocation unknowns. The Lobatto IIIa scheme then applies Newton corrections to this initial profile under adaptive mesh refinement until the residual tolerance is satisfied. Thus, the exponentially decaying functions are not used as a separate time-marching Runge–Kutta trajectory; they initialise the nonlinear collocation solve.

3.2 Verification

To verify the numerical implementation, we compare with published benchmark data in several limiting cases.

IJMSO

International Journal of Mathematical Sciences and Optimization: Theory and Applications
12(1), 2026, Pages 104 - 128
https://doi.org/10.5281/zenodo.20467246

Exact solution verification. In the flat plate limit ($\gamma = 0$) with no porous medium, chemical reaction, stratification, buoyancy, unsteadiness, or suction ($Da = K_a = K = S = F = \lambda_T = Nr = A = f_w = 0$, $\bar{\gamma} = 1$), the momentum equation reduces to the classical Crane [39] stretching sheet problem:

$$f''' + f\,f'' - (f')^2 = 0, \qquad f(0) = 0,\ f'(0) = 1,\ f'(\infty) = 0, \tag{3.11}$$

which admits the exact closed-form solution $f(\eta) = 1 - e^{-\eta}$, yielding $f''(0) = -1$ exactly. Our solver reproduces $f''(0) = -1.000000$ to six decimal places, confirming the correctness of the momentum equation implementation.

Comparison with published benchmarks. Table 1 compares $f''(0)$ and $\theta(0)$ with the published results of Elbashbeshy [44], Bachok and Ishak [43], and Ishak et al. [42] for the limiting stretching cylinder problem. The fundamental axisymmetric flow was first studied by Wang [40]. Three values of the curvature parameter ($\gamma = 0, 0.5, 1$) are considered.

Table 1: Comparison of $f''(0)$ and $\theta(0)$ with published benchmarks.

		$\theta(0)$			$f''(0)$	
γ	Pr	[44]	[43]	Present	[39]	Present
0	0.72	1.2253	1.2367	1.236649	−1.0000	−1.000000
	1	1.0000	1.0000	1.000000	(exact)	−1.000000
	6.7	–	0.3333	0.333303		−1.000000
	10	0.2688	0.2688	0.268769		−1.000000
0.5	0.72	–	–	1.005806	–	−1.180665
	1	–	–	0.846980		−1.180665
	6.7	–	–	0.313686		−1.180665
	10	–	–	0.255784		−1.180665
1	0.72	–	0.8701	0.853168	–	−1.353302
	1	–	0.7439	0.738933		−1.353302
	6.7	–	0.2966	0.296835		−1.353302
	10	–	0.2442	0.244307		−1.353302

Table 1 shows close agreement with the benchmark data for $\gamma = 0$ (flat plate limit). For $\gamma = 1$, the deviations of order $\sim 2\%$ relative to Bachok and Ishak are attributable to differences in far-field truncation and mesh resolution.

Beyond the tabulated benchmark comparisons, the predicted directional trends with respect to curvature and effective transport parameters are also consistent with more recent porous-cylinder and anisotropic-porous studies reported in the literature (e.g., [12, 41]), providing an additional qualitative verification layer for the present implementation.

Several physical consistency features are worth noting. The wall shear stress $f''(0)$ depends solely on γ and is independent of Pr, as expected from the one-way coupling of the momentum equation in this limiting case. Increasing the curvature parameter from $\gamma = 0$ to $\gamma = 1$ increases $|f''(0)|$ from 1.0000 to 1.3533, reflecting the enhanced velocity gradient near a curved surface. For each γ, $\theta(0)$ decreases monotonically with increasing Pr, consistent with a thinner thermal boundary layer at higher Prandtl numbers.

Grid independence. Grid independence was verified by varying the number of mesh nodes N and the far-field truncation $\eta_{\max}$. Increasing N from 200 to 400 altered the engineering quantities by less than 10^{-5}, while extending $\eta_{\max}$ from 10 to 15 produced changes smaller than 10^{-6}. The decay conditions $f'(\eta_{\max}), \theta(\eta_{\max}), \phi(\eta_{\max}) < 10^{-6}$ were confirmed for all cases.

IJMSO

International Journal of Mathematical Sciences and Optimization: Theory and Applications
12(1), 2026, Pages 104 - 128
https://doi.org/10.5281/zenodo.20467246

4 Results and discussion

The BVP Equation (2.30)–Equation (2.34) is solved for a range of governing parameters. Unless otherwise stated, the baseline values are:

$$A = 0.3,\ \bar{\gamma} = 0.3,\ \gamma = 1,\ Da = 6,\ \lambda_T = 3,\ Nr = 0.8,\ K_a = 0.5,$$
$$Pr = 0.71,\ n = 1,\ S = 0.5,\ Sc = 0.22,\ K = 0.6,\ F = 0.5,\ f_w = 0.5.$$

4.1 Tabulated engineering quantities

Table 2: Engineering quantities for varying A, $\bar{\gamma}$, γ, and Da.

A	$\bar{\gamma}$	γ	Da	$f''(0)$	$\theta(0)$	$-\phi'(0)$
0.3	0.3	1.0	6	−1.7873	0.5274	1.1182
0.5				−1.9159	0.5283	1.1236
0.7				−2.0417	0.5288	1.1291
0.3	0.1			−2.5964	0.5367	1.1118
	0.2			−2.0206	0.5315	1.1153
	0.4			−1.6527	0.5239	1.1206
	0.3	0.4		−1.3647	0.6118	0.8811
		0.6		−1.5152	0.5801	0.9623
		0.8		−1.6553	0.5522	1.0411
		1.0	8	−2.3998	0.5580	1.0977
			10	−2.9416	0.5845	1.0812
			12	−3.4298	0.6078	1.0676

From Table 2, the following trends are observed. Increasing A monotonically increases $|f''(0)|$ and produces a mild increase in both $\theta(0)$ and $-\phi'(0)$, reflecting the role of temporal inertia in modifying the velocity gradient at the wall. Decreasing $\bar{\gamma}$, corresponding to weaker effective viscosity, increases $|f''(0)|$ substantially, from 1.65 at $\bar{\gamma} = 0.4$ to 2.60 at $\bar{\gamma} = 0.1$, confirming that the wall shear stress is highly sensitive to the effective viscosity within the porous matrix. The curvature parameter γ reduces $\theta(0)$ significantly: increasing γ from 0.4 to 1.0 lowers $\theta(0)$ from 0.6118 to 0.5274, a 13.8% decrease consistent with enhanced radial diffusion at higher curvatures. Meanwhile, $-\phi'(0)$ increases from 0.88 to 1.12 over the same range, indicating that the stronger radial spreading steepens the concentration gradient. The porous drag parameter Da increases $|f''(0)|$ monotonically from 1.79 at $Da = 6$ to 3.43 at $Da = 12$, reflecting the growing porous resistance; simultaneously, $\theta(0)$ rises, indicating weaker heat transfer, while $-\phi'(0)$ slightly decreases, showing that the porous resistance retards convective mass transport.

IJMSO

International Journal of Mathematical Sciences and Optimization: Theory and Applications
12(1), 2026, Pages 104 - 128
https://doi.org/10.5281/zenodo.20467246

Table 3: Engineering quantities for varying Sc, K, and F (with $A = 0.1$).

Sc	K	F	$f''(0)$	$\theta(0)$	$-\phi'(0)$
0.22	0.6	0.5	−1.6560	0.5261	1.1128
0.60	0.6	0.5	−1.7961	0.5639	1.6896
0.78	0.6	0.5	−1.8495	0.5758	1.9205
0.22	0.0	0.5	−1.6257	0.5156	0.9939
0.22	0.3	0.5	−1.6415	0.5211	1.0557
0.22	0.6	0.5	−1.6560	0.5261	1.1128
0.22	1.0	0.5	−1.6736	0.5321	1.1830
0.22	0.6	0.2	−1.6440	0.5224	1.0657
0.22	0.6	0.5	−1.6560	0.5261	1.1128
0.22	0.6	0.8	−1.6676	0.5298	1.1587

Table 3 isolates the solutal transport parameters. Increasing Sc from 0.22 to 0.78 increases $-\phi'(0)$ from 1.11 to 1.92, a $\sim 73\%$ increase that reflects the classical thinning of the concentration boundary layer at higher Schmidt numbers. The chemical reaction parameter K produces a monotonic increase in $-\phi'(0)$: from 0.994 at $K = 0$ to 1.183 at $K = 1.0$, confirming that the destructive reaction consumes species within the boundary layer and steepens the wall concentration gradient. This $\sim 19\%$ increase shows that chemical reaction controls mass transfer rates. The solutal stratification parameter F also produces a monotonic increase in $-\phi'(0)$, since higher stratification reduces the effective concentration driving force and promotes a steeper near-wall gradient.

4.2 Parametric study

To improve readability, the discussion below is organised by parameter families (inertial/viscous, buoyancy/stratification, transport-property, and porous-medium controls), with emphasis on the governing mechanisms and engineering implications rather than repeated curve-by-curve narration.

4.2.1 Effect of the unsteadiness parameter A.

Figure 2 displays the velocity, temperature, and concentration profiles for several values of A. Increasing A suppresses the velocity field within the momentum boundary layer; physically, a larger A introduces additional temporal inertia through the terms $A\,f'$ and $\frac{1}{2}A\,\eta\,f''$ in Equation (2.30), which oppose the buoyancy-driven acceleration. The corresponding reduction in convective intensity produces thinner thermal and solutal boundary layers, as evident in the $\theta(\eta)$ and $\phi(\eta)$ profiles. From Table 2, $|f''(0)|$ increases from 1.79 to 2.04 over $A \in [0.3, 0.7]$, indicating that the steeper velocity gradient near the wall is a consequence of the stronger inertial retardation of the outer flow.

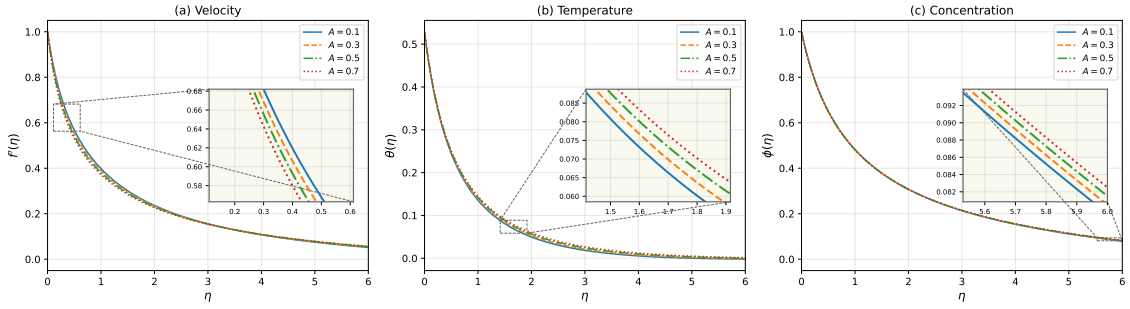

Figure 2: Effect of A on velocity, temperature, and concentration profiles.

IJMSO
International Journal of Mathematical Sciences and Optimization: Theory and Applications
12(1), 2026, Pages 104 - 128
https://doi.org/10.5281/zenodo.20467246

4.2.2 Effect of the viscosity ratio $\bar{\gamma}$.

Figure 3 shows the influence of the viscosity ratio $\bar{\gamma} = \nu_{\text{eff}}/\nu$, which measures the effective viscous diffusion within the porous matrix relative to the clear-fluid viscosity. A higher $\bar{\gamma}$ amplifies the diffusion operator $\bar{\gamma}[(1 + 2\gamma\eta)\, f''' + 2\gamma\, f'']$ in Equation (2.30), allowing momentum to diffuse more readily across the boundary layer. Consequently, the velocity profile flattens and the peak velocity weakens with increasing $\bar{\gamma}$. The reduced convective transport produces lower thermal and solutal gradients at the wall. From Table 2, decreasing $\bar{\gamma}$ from 0.4 to 0.1 increases $|f''(0)|$ from 1.65 to 2.60, a 57% rise, showing that wall shear stress is sensitive to the effective viscosity in porous media.

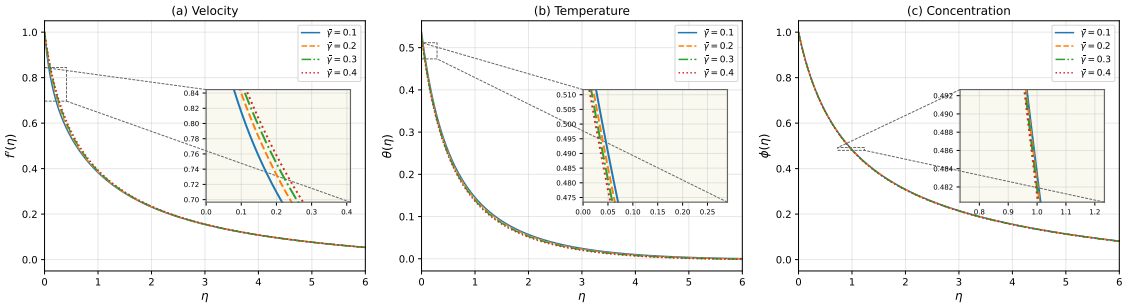

Figure 3: Effect of $\bar{\gamma}$ on velocity, temperature, and concentration profiles.

4.2.3 Effect of the chemical reaction parameter K.

The chemical reaction parameter K appears as the sink term $-K\,\phi$ in the species equation Equation (2.32), where $K > 0$ corresponds to a destructive first-order chemical reaction. As shown in Figure 4, increasing K reduces $\phi(\eta)$: the reaction progressively consumes the diffusing species within the boundary layer, driving the concentration toward zero more rapidly and producing a steeper wall gradient. From Table 3, $-\phi'(0)$ increases monotonically from 0.994 at $K = 0$ to 1.183 at $K = 1.0$, a $\sim 19\%$ increase in mass transfer. The velocity field is mildly retarded because the solutal buoyancy contribution $Nr\,\phi$ in Equation (2.30) weakens as the concentration decays faster under stronger reaction. Temperature profiles are also slightly affected through the velocity–energy coupling.

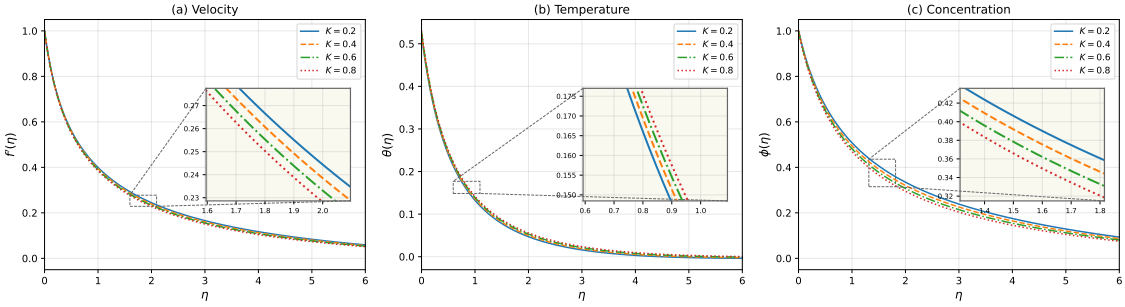

Figure 4: Effect of K on velocity, temperature, and concentration profiles.

4.2.4 Effect of the thermal buoyancy parameter λ_T.

Figure 5 demonstrates that increasing λ_T accelerates the fluid, as expected from the positive coupling term $\lambda_T(\theta + Nr\,\phi)$ in Equation (2.30). A larger λ_T amplifies the buoyancy force generated by both the thermal and solutal concentration fields, producing a fuller velocity profile. The higher

IJMSO
International Journal of Mathematical Sciences and Optimization: Theory and Applications
12(1), 2026, Pages 104 - 128
https://doi.org/10.5281/zenodo.20467246

convective velocities carry heat and species away from the surface, steepening the near-wall gradients in $\theta(\eta)$ and $\phi(\eta)$. The temperature profiles thin noticeably because the advection term $f\,\theta'$ grows with f, while the solutal profiles respond similarly through $f\,\phi'$.

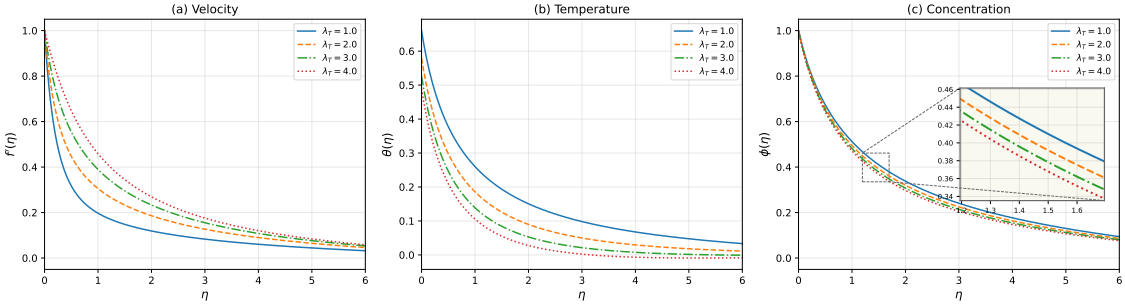

Figure 5: Effect of λ_T on velocity, temperature, and concentration profiles.

4.2.5 Effect of the solutal stratification parameter F.

The solutal stratification parameter F enters the species equation Equation (2.32) through the source term $-F\,f'$, which accounts for the linear variation of the ambient concentration with height. Increasing F (Figure 6) reduces the effective concentration difference between the surface and the far field, causing the concentration distribution $\phi(\eta)$ to decay more rapidly. The resulting thinner concentration boundary layer produces a steeper wall gradient and hence a higher Sherwood number, consistent with the monotonic increase of $-\phi'(0)$ from 1.066 to 1.159 over $F \in [0.2, 0.8]$ in Table 3. The velocity field is only weakly affected because F does not appear directly in the momentum equation; however, the solutal buoyancy coupling $Nr\,\phi$ provides an indirect influence.

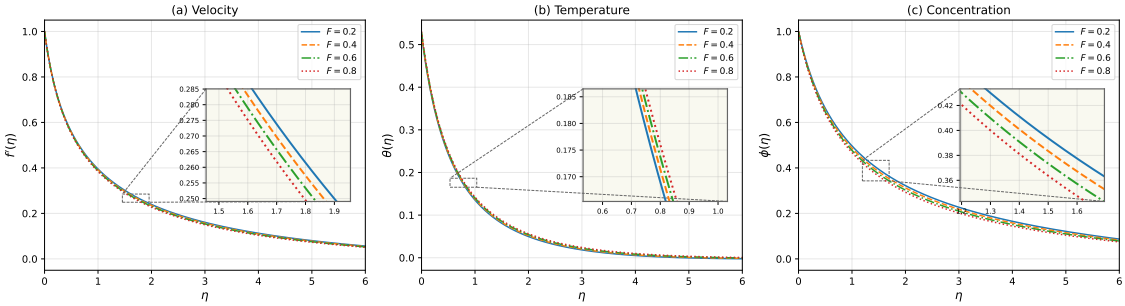

Figure 6: Effect of F on velocity, temperature, and concentration profiles.

4.2.6 Effect of the buoyancy ratio Nr.

The buoyancy ratio $Nr = \lambda_C/\lambda_T$ quantifies the relative strength of the solutal buoyancy force to the thermal buoyancy force. Increasing Nr (Figure 7) adds a larger solutal contribution to the momentum equation through the term $\lambda_T\,Nr\,\phi$, which accelerates the flow. The resulting higher convective velocities enhance both thermal and solutal transport: the thermal boundary layer thins because the advection term $f\,\theta'$ intensifies, and the concentration boundary layer responds similarly through $f\,\phi'$. Since the buoyancy ratio couples directly with the concentration field through $\lambda_T\,Nr\,\phi$, the effect on $\phi(\eta)$ is strongest.

IJMSO
International Journal of Mathematical Sciences and Optimization: Theory and Applications
12(1), 2026, Pages 104 - 128
https://doi.org/10.5281/zenodo.20467246

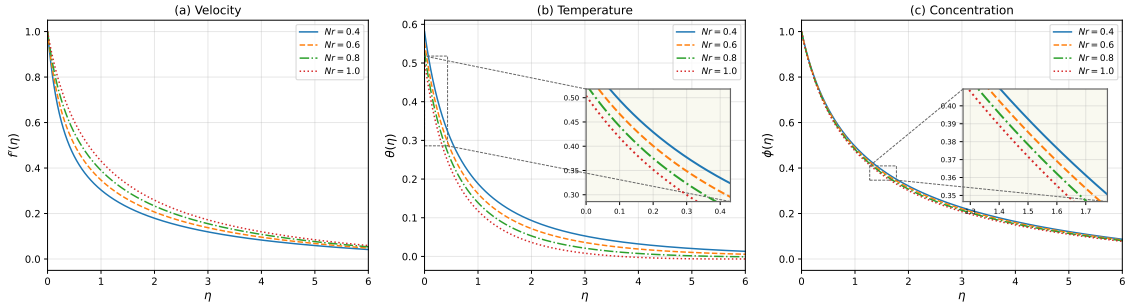

Figure 7: Effect of Nr on velocity, temperature, and concentration profiles.

4.2.7 Effect of the thermal stratification parameter S.

The thermal stratification parameter S represents the linear increase of the ambient temperature with height and appears as $-S\,f'$ in the energy equation Equation (2.31). Increasing S (Figure 8) weakens the effective temperature difference between the heated surface and the far field, reducing $\theta(\eta)$ and thinning the thermal boundary layer. Since the Nusselt number is proportional to $1/\theta(0)$ under the prescribed-flux boundary condition (see Section 2), the decrease in $\theta(0)$ implies enhanced heat transfer. The velocity field is indirectly affected through the thermal buoyancy term $\lambda_T\,\theta$ in Equation (2.30): a smaller θ weakens the buoyancy driving force, slightly decelerating the flow.

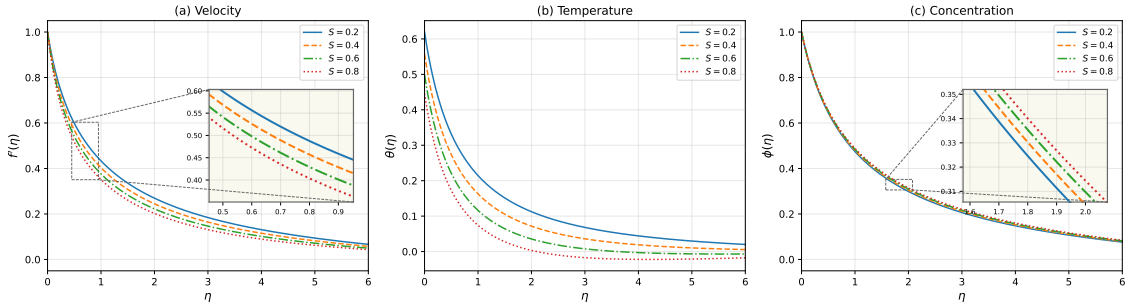

Figure 8: Effect of S on velocity, temperature, and concentration profiles.

4.2.8 Effect of the Schmidt number Sc.

The Schmidt number $Sc = \nu/D_m$ measures the ratio of momentum to mass diffusivity. Increasing Sc (Figure 9) reduces the mass diffusivity, causing the concentration boundary layer to become much thinner than the momentum or thermal boundary layers. The sharper drop in $\phi(\eta)$ near the wall produces a steeper wall gradient and a higher Sherwood number. From Table 3, $-\phi'(0)$ increases from 1.11 at $Sc = 0.22$ to 1.92 at $Sc = 0.78$, a $\sim 73\%$ enhancement. The velocity field is also affected: a higher Sc concentrates the species near the surface, strengthening the solutal buoyancy coupling $Nr\,\phi$ in the near-wall region and slightly increasing $|f''(0)|$.

IJMSO

International Journal of Mathematical Sciences and Optimization: Theory and Applications
12(1), 2026, Pages 104 - 128
https://doi.org/10.5281/zenodo.20467246

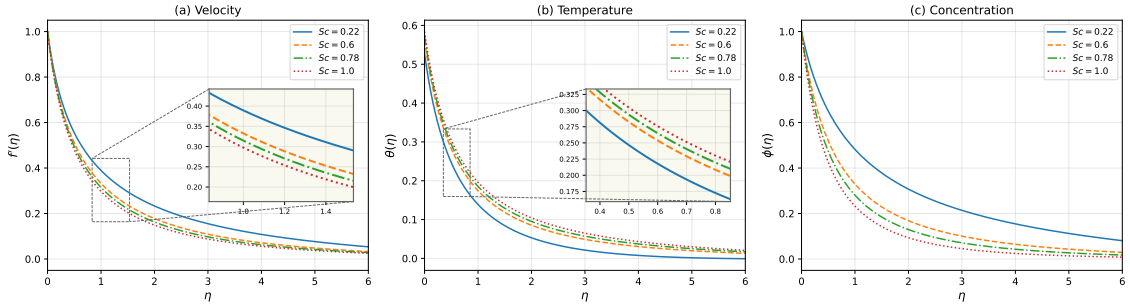

Figure 9: Effect of Sc on velocity, temperature, and concentration profiles.

4.2.9 Effect of the anisotropic permeability parameter K_a.

The anisotropic permeability parameter $K_a = k^* \sin^2\theta^* + \cos^2\theta^*$ quantifies the directional resistance of the porous medium; a larger K_a implies greater flow resistance along the cylinder axis. Increasing K_a intensifies the drag term $K_a\, Da\, f'$ in Equation (2.30), which directly opposes the fluid velocity. As shown in Figure 10, the velocity profile is suppressed, and the resulting reduction in convective intensity produces thicker thermal and solutal boundary layers. The orientation of the anisotropy principal axes relative to the flow direction is therefore a control parameter: even moderate changes in K_a produce noticeable alterations in all three transport fields.

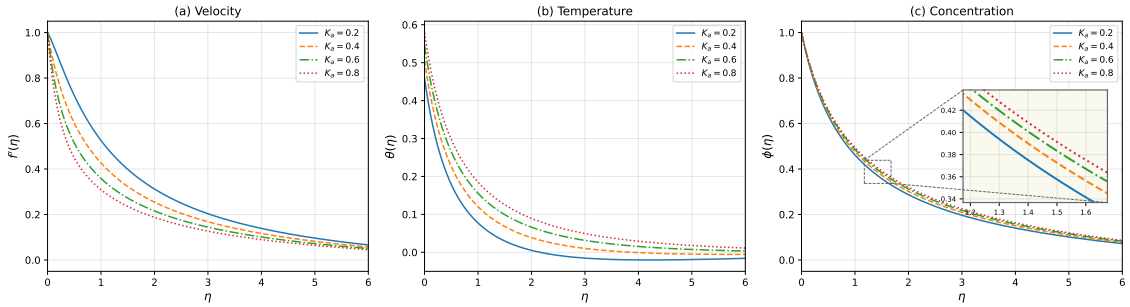

Figure 10: Effect of K_a on velocity, temperature, and concentration profiles.

4.2.10 Effect of suction/injection f_w.

The parameter f_w controls the transpiration velocity at the cylinder surface: $f_w > 0$ corresponds to suction (fluid removal) and $f_w < 0$ to injection (fluid blowing). Figure 11 shows that suction thins all three boundary layers by removing warmer and more concentrated fluid from the near-wall region, which steepens the velocity, temperature, and concentration gradients at the surface. Conversely, injection ($f_w < 0$) thickens the layers by advecting fluid outward, reducing wall gradients. The contrast between the $f_w = -0.5$ and $f_w = 0.5$ profiles is large, confirming that surface transpiration controls heat and mass transfer rates in stratified porous systems.

IJMSO

International Journal of Mathematical Sciences and Optimization: Theory and Applications
12(1), 2026, Pages 104 - 128
https://doi.org/10.5281/zenodo.20467246

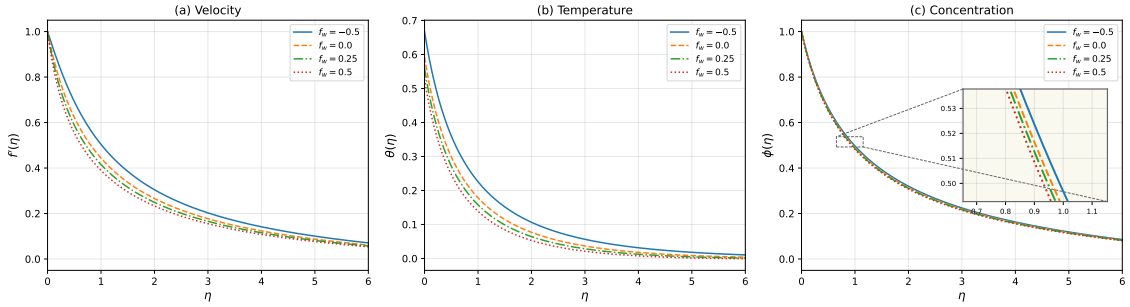

Figure 11: Effect of f_w on velocity, temperature, and concentration profiles.

4.2.11 Effect of the Prandtl number Pr.

The Prandtl number $Pr = \nu/\alpha$ determines the relative thickness of the momentum and thermal boundary layers. Increasing Pr (Figure 12) reduces the thermal diffusivity, producing a thinner thermal boundary layer that lies well inside the momentum layer. The steeper temperature gradient at the wall directly enhances the local Nusselt number ($Nu \propto 1/\theta(0)$). At $Pr = 7$ (water), the thermal boundary layer is markedly thinner than at $Pr = 0.71$ (air), and $\theta(0)$ is reduced accordingly. The concentration and velocity profiles are only weakly affected because Pr does not appear explicitly in the species or momentum equations; the influence propagates indirectly through the buoyancy term $\lambda_T\,\theta$.

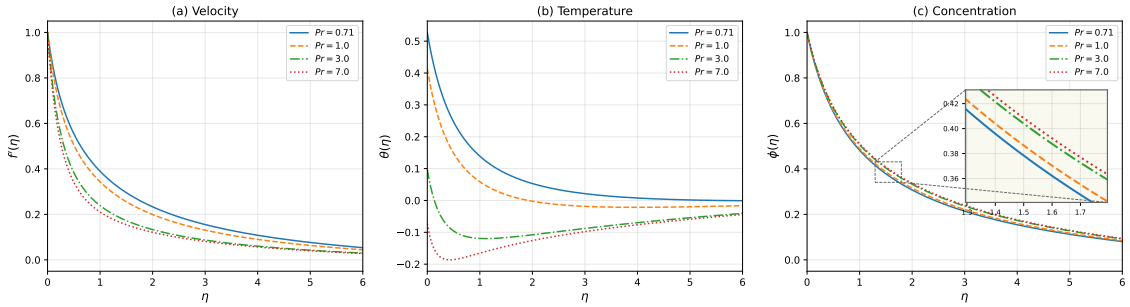

Figure 12: Effect of Pr on velocity, temperature, and concentration profiles.

4.2.12 Effect of the curvature parameter γ.

The curvature parameter $\gamma = (1/a)\sqrt{\nu z/U_w}$ measures the relative importance of transverse curvature in the diffusion operators. For a flat plate, $\gamma = 0$ and the curvature terms vanish; for a slender cylinder, γ is large. Higher γ enhances the effective radial diffusion through the $(1+2\gamma\eta)$ factor that multiplies the second derivatives in Equations (2.30) to (2.32), plus the additional first-derivative terms $2\gamma\, f''$, $2\gamma\,\theta'$, and $2\gamma\,\phi'$. As shown in Figure 13, all three boundary layers thin monotonically with increasing γ. From Table 2, $\theta(0)$ decreases from 0.612 ($\gamma = 0.4$) to 0.527 ($\gamma = 1.0$), a 13.8% reduction in the surface temperature that corresponds to a 16.0% enhancement in the Nusselt number ($Nu \propto 1/\theta(0)$) over this range.

IJMSO
International Journal of Mathematical Sciences and Optimization: Theory and Applications
12(1), 2026, Pages 104 - 128
https://doi.org/10.5281/zenodo.20467246

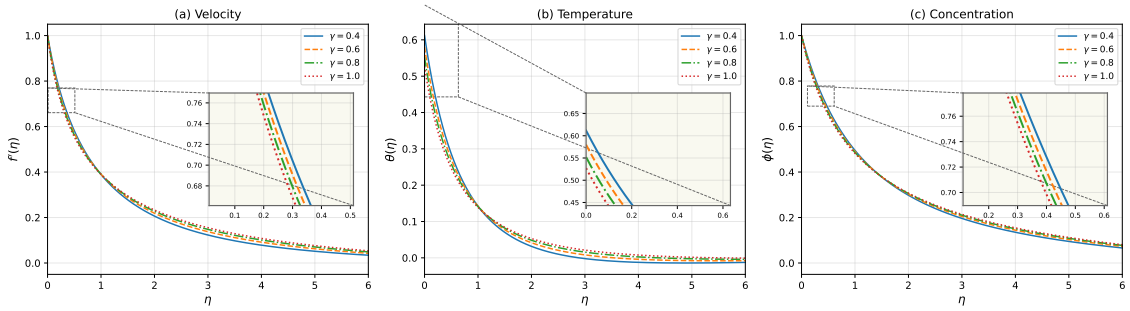

Figure 13: Effect of γ on velocity, temperature, and concentration profiles.

4.2.13 Effect of the porous drag parameter Da.

The porous drag parameter $Da = \nu z/(k_1 U_w)$ quantifies the ratio of viscous drag to the porous medium permeability; a larger Da implies stronger resistance to flow through the porous matrix. Figure 14 shows that increasing Da suppresses the velocity field progressively, because the drag term $K_a\, Da\, f'$ in Equation (2.30) grows linearly with Da. From Table 2, $|f''(0)|$ nearly doubles from 1.79 at $Da = 6$ to 3.43 at $Da = 12$, reflecting the strongly retarded near-wall flow. The reduced convective velocities weaken advective transport of heat and species, causing $\theta(0)$ to increase, corresponding to a lower Nusselt number, and $-\phi'(0)$ to decrease slightly, corresponding to a lower Sherwood number. These trends demonstrate that the porous medium resistance acts as a strong damping mechanism on all three transport processes simultaneously.

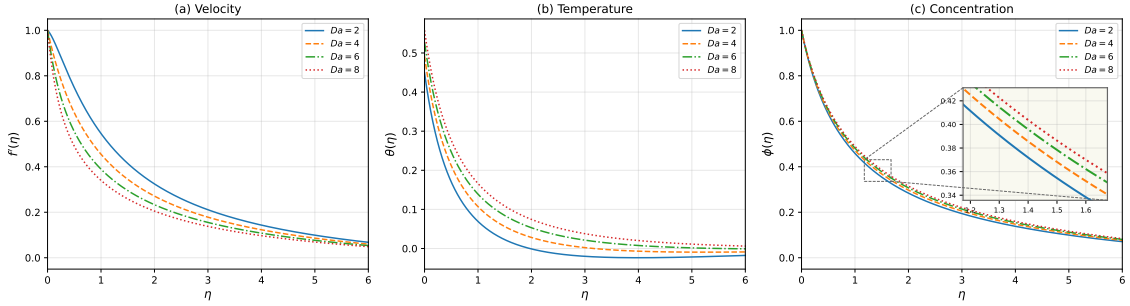

Figure 14: Effect of Da on velocity, temperature, and concentration profiles.

From an application perspective, these trends indicate distinct design levers across target systems: in geothermal extraction, reducing effective porous resistance helps preserve convective heat transport; in enhanced oil recovery, tuning reaction intensity and suction/injection can selectively strengthen species removal without proportionally increasing thermal losses; and in groundwater contaminant transport, stratification parameters and Schmidt-number-controlled diffusivity regulate plume thickness and near-boundary mass flux.

4.3 Global sensitivity analysis

To quantify the relative influence of each governing parameter on the engineering quantities, a global sensitivity analysis is performed using Latin Hypercube Sampling (LHS). The sampled parameter ranges are chosen to span physically admissible values used in the computational study and in related porous-convection literature: $A \in [0, 0.6]$, $\bar{\gamma} \in [0.1, 0.6]$, $\gamma \in [0, 2]$, $Da \in [1, 12]$, $\lambda_T \in [0.5, 6]$, $Nr \in [0.1, 1.5]$, $K_a \in [0.2, 1]$, $Pr \in [0.3, 7]$, $n \in [0.5, 2]$, $S \in [0, 1]$, $Sc \in [0.1, 2]$, $K \in [0, 1.5]$, $F \in [0, 1]$, and $f_w \in [0, 1]$. A total of 500 LHS samples is used as a compromise between statistical

IJMSO

International Journal of Mathematical Sciences and Optimization: Theory and Applications
12(1), 2026, Pages 104 - 128
https://doi.org/10.5281/zenodo.20467246

coverage and BVP computational cost; in practice, the ranking of dominant parameters remained stable under additional trial runs with nearby sample sizes. For each sample, the BVP is solved and the quantities $f''(0)$, $\theta(0)$, and $-\phi'(0)$ are recorded. The Spearman rank correlation coefficient r_s between each parameter and each output is then computed; its absolute value measures the strength of monotonic association, while its sign indicates the direction. The normalised percentage influence is defined as $\%_i = 100\,|r_{s,i}|/\sum_j |r_{s,j}|$.

Because Spearman analysis measures monotonic dependence, two limitations should be noted: it does not capture strongly non-monotonic interactions and it does not by itself provide causal direction. Therefore, the sensitivity rankings are interpreted together with the physics-based parametric trends discussed in Section 4.

Table 4: Spearman rank correlations and normalised percentage influence (500 LHS samples).

	$\theta(0)$		$-\phi'(0)$		$f''(0)$	
Parameter	r_s	%	r_s	%	r_s	%
Pr	−0.762	33.9	−0.017	0.7	−0.268	9.6
Sc	+0.011	0.5	+0.861	36.5	−0.138	4.9
f_w	−0.159	7.1	+0.212	9.0	−0.286	10.3
S	−0.508	22.6	−0.033	1.4	−0.044	1.6
λ_T	−0.098	4.4	+0.143	6.1	+0.376	13.5
Da	+0.152	6.7	+0.002	0.1	−0.450	16.2
γ	−0.034	1.5	+0.404	17.1	−0.086	3.1
K_a	+0.097	4.3	−0.071	3.0	−0.389	14.0
Nr	−0.102	4.5	+0.064	2.7	+0.362	13.0
$\tilde{\gamma}$	−0.144	6.4	+0.032	1.4	+0.252	9.0
K	+0.068	3.0	+0.265	11.2	−0.000	0.0
F	−0.024	1.1	+0.134	5.7	+0.070	2.5
n	+0.074	3.3	−0.104	4.4	+0.005	0.2
A	−0.011	0.5	−0.016	0.7	−0.061	2.2

Table 4 reveals three distinct groups of dominant parameters, visualised in Figure 15:

IJMSO
International Journal of Mathematical Sciences and Optimization: Theory and Applications
12(1), 2026, Pages 104 - 128
https://doi.org/10.5281/zenodo.20467246

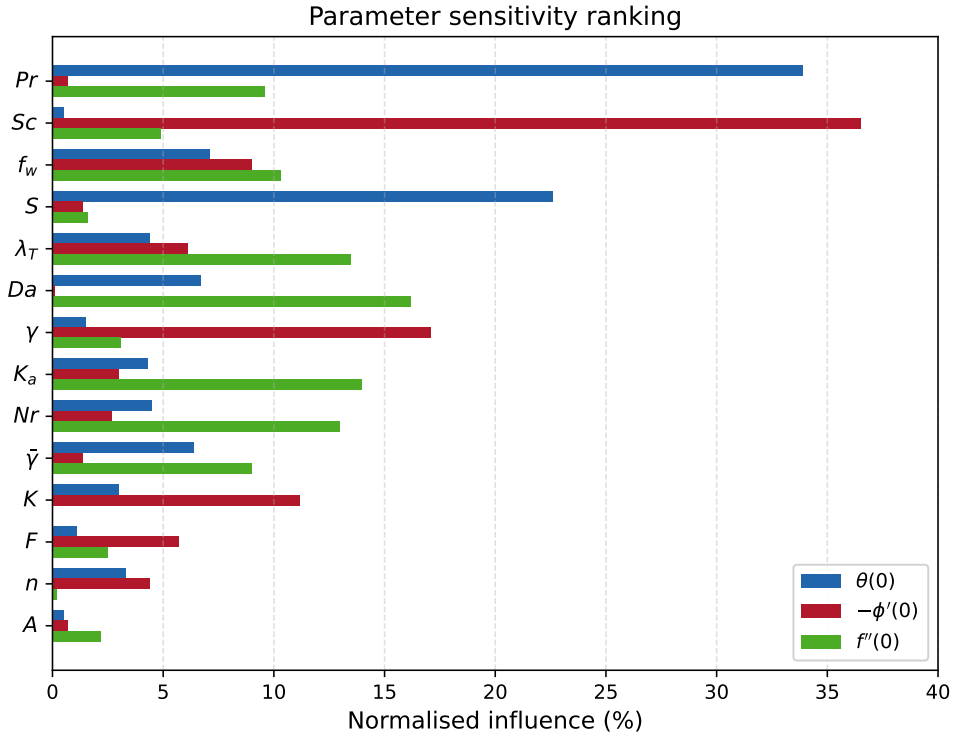

Figure 15: Normalised percentage influence of each parameter on the engineering quantities.

For the temperature field $\theta(0)$, the Prandtl number is the single most influential parameter ($r_s = -0.762$, 33.9%), followed by the thermal stratification parameter S ($r_s = -0.508$, 22.6%). The strong negative correlations indicate that higher Pr and S both reduce $\theta(0)$, corresponding to enhanced Nusselt numbers. The suction parameter f_w contributes 7.1%, while the remaining parameters each account for less than 7%.

For mass transfer $-\phi'(0)$, the Schmidt number dominates overwhelmingly ($r_s = +0.861$, 36.5%), reflecting the direct role of species diffusivity in controlling the Sherwood number. The curvature parameter γ ranks second (17.1%), followed by the chemical reaction parameter K (11.2%) and the suction parameter f_w (9.0%).

For skin friction $f''(0)$, the porous drag parameter Da ($r_s = -0.450$, 16.2%), the anisotropic permeability parameter K_a (14.0%), and the thermal buoyancy parameter λ_T (13.5%) are the three most influential parameters, all of comparable magnitude. The buoyancy ratio Nr (13.0%), suction parameter f_w (10.3%), and Prandtl number (9.6%) provide secondary contributions.

A noteworthy outcome is the cross-coupling structure: the unsteadiness parameter A has uniformly weak influence ($< 2.5\%$) on all three quantities, indicating that steady-state solutions provide reasonable approximations under the conditions studied. In contrast, the suction parameter f_w appears consistently in the top-five most influential parameters for all three engineering quantities, underscoring its practical importance as a boundary control mechanism.

5 Conclusions

The combined effects of a first-order chemical reaction and anisotropic porous permeability on unsteady free convection boundary layer flow past a vertically translating circular cylinder have been investigated under simultaneous linear thermal and solutal stratifications. The governing PDEs were reduced to a seventh-order coupled nonlinear ODE system via similarity transformations

IJMSO

International Journal of Mathematical Sciences and Optimization: Theory and Applications
12(1), 2026, Pages 104 - 128
https://doi.org/10.5281/zenodo.20467246

and solved numerically by the Lobatto IIIa collocation method, with verification against published benchmarks.

The principal findings are as follows. Increasing the unsteadiness parameter A suppresses all three boundary layer profiles, with $|f''(0)|$ rising from 1.79 to 2.04 over $A \in [0.3, 0.7]$ due to stronger temporal inertia. The chemical reaction parameter K exerts a monotonic effect on the concentration field: increasing K from 0 to 1.0 enhances the Sherwood number $-\phi'(0)$ by $\sim 19\%$, confirming that the destructive reaction steepens the wall concentration gradient. Higher Schmidt number thins the concentration boundary layer and increases the surface mass transfer rate, with $-\phi'(0)$ rising by $\sim 73\%$ over $Sc \in [0.22, 0.78]$. Surface suction simultaneously reduces all boundary layer thicknesses and enhances the skin-friction coefficient, Nusselt number, and Sherwood number, while injection has the opposite effect. Thermal stratification suppresses the temperature field but enhances the Nusselt number through boundary layer thinning, consistent with the prescribed-flux interpretation $Nu \propto 1/\theta(0)$. The anisotropic permeability parameter K_a and the porous drag parameter Da govern momentum diffusion; $|f''(0)|$ nearly doubles from 1.79 to 3.43 as Da increases from 6 to 12, while porous drag simultaneously suppresses convective heat and mass transport. The viscosity ratio $\bar{\gamma}$ has the greatest influence on the wall shear stress: decreasing $\bar{\gamma}$ from 0.4 to 0.1 increases $|f''(0)|$ from 1.65 to 2.60, a 57% rise.

These results bear directly on transport processes in stratified porous environments. In petroleum reservoirs, the combined influence of chemical reactions and anisotropic permeability controls species migration during enhanced oil recovery; the quantitative relationships between K, K_a, and the Sherwood number provide a basis for optimising catalytic transport in layered reservoir formations. In geothermal systems, anisotropic permeability is a property of sedimentary rock formations; the parametric trends identified here, particularly the sensitivity of the Nusselt number and wall shear to $\bar{\gamma}$, γ, and Da, are relevant to the design of extraction and reinjection systems. In environmental engineering, the interplay of solutal stratification, chemical reaction, and surface suction governs contaminant dispersion in groundwater systems.

Several modelling assumptions bound the applicability of these results. The similarity transformation requires specific power-law forms for the wall velocity $U_w(z,t)$ and the surface heat flux $q_w(z,t)$; arbitrary wall conditions would necessitate a non-similar solution. The analysis is restricted to laminar, axisymmetric boundary layer flow, so transition to turbulence or three-dimensional instabilities at higher Grashof numbers is not captured. The Boussinesq approximation limits validity to small temperature and concentration variations relative to their reference values, excluding large-gradient regimes. A first-order irreversible chemical reaction is assumed; higher-order kinetics, reversible reactions, or multi-step mechanisms may alter the concentration field qualitatively. Thermal radiation, viscous dissipation, and Soret/Dufour cross-diffusion effects are neglected, and their inclusion could modify the energy and species balance in high-temperature or high-concentration applications.

Extensions to non-Newtonian rheologies, higher-order chemical kinetics, and three-dimensional geometries are the subject of ongoing work.

Declaration of competing interest

The authors declare that they have no known competing financial interests or personal relationships that could have appeared to influence the work reported in this paper.

Data availability

The data that support the findings of this study are available within the article. The source code used to generate the results will be made available upon reasonable request to the corresponding author.

IJMSO

International Journal of Mathematical Sciences and Optimization: Theory and Applications
12(1), 2026, Pages 104 - 128
https://doi.org/10.5281/zenodo.20467246

6 Nomenclature

Dimensional quantities

Symbol	Description (SI unit)
a	Radius of the circular cylinder (m)
b	Velocity constant, $b = U/l$ (s^{-1})
C	Species concentration ($\mathrm{kg\,m}^{-3}$)
C_w, C_∞	Wall and ambient species concentrations ($\mathrm{kg\,m}^{-3}$)
C_p	Specific heat at constant pressure ($\mathrm{J\,kg}^{-1}\,\mathrm{K}^{-1}$)
D_m	Mass diffusivity ($\mathrm{m}^2\,\mathrm{s}^{-1}$)
g	Gravitational acceleration ($\mathrm{m\,s}^{-2}$)
k	Thermal conductivity ($\mathrm{W\,m}^{-1}\,\mathrm{K}^{-1}$)
k_1, k_2	Principal permeabilities (m^2)
K_{11}, K_{12}, K_{22}	Components of the permeability tensor (m^2)
$\bar{\bar{K}}$	Symmetric permeability tensor
K_r	Chemical reaction rate constant (s^{-1})
l	Characteristic length (m)
q_w, q_{w0}	Surface and reference heat flux ($\mathrm{W\,m}^{-2}$)
r, z	Radial and axial coordinates (m)
$\boldsymbol{R}(\theta^*)$	Planar rotation matrix
S_1, S_2	Dimensional stratification parameters
t	Time (s)
T, T_w, T_∞	Fluid, wall, and ambient temperatures (K)
$\boldsymbol{v}$	Velocity vector, $\boldsymbol{v} = (u, v)$ ($\mathrm{m\,s}^{-1}$)
u, v	Axial and radial velocity components ($\mathrm{m\,s}^{-1}$)
U, U_w, V_w	Reference, surface, and suction/injection velocities ($\mathrm{m\,s}^{-1}$)

Greek symbols

Symbol	Description (SI unit)
α	Thermal diffusivity, $k/(\rho C_p)$ ($\mathrm{m}^2\,\mathrm{s}^{-1}$)
β, β^*	Thermal and solutal expansion coefficients (K^{-1}, $\mathrm{m}^3\,\mathrm{kg}^{-1}$)
λ	Temporal decay constant (s^{-1})
ν, ν_{eff}	Kinematic and effective kinematic viscosities ($\mathrm{m}^2\,\mathrm{s}^{-1}$)
ρ, ρ_∞	Fluid and ambient densities ($\mathrm{kg\,m}^{-3}$)
θ^*	Inclination angle of anisotropic principal axis (rad)
ψ	Stream function ($\mathrm{m}^2\,\mathrm{s}^{-1}$)

IJMSO

International Journal of Mathematical Sciences and Optimization: Theory and Applications
12(1), 2026, Pages 104 - 128
https://doi.org/10.5281/zenodo.20467246

Dimensionless variables and parameters

Symbol	Description
η	Similarity variable
$\eta_{\max}$	Far-field truncation point
f, f', θ, ϕ	Dimensionless stream function, velocity, temperature, concentration
A	Unsteadiness parameter (λ/b)
n	Heat flux exponent
K_a	Anisotropic permeability parameter
k^*	Permeability ratio (k_1/k_2)
Da	Porous drag parameter
F, S	Solutal and thermal stratification parameters
K	Chemical reaction parameter
Nr	Buoyancy ratio
Pr, Sc	Prandtl and Schmidt numbers
Re_z	Local Reynolds number (zU_w/ν)
Gr_z, Gc_z	Local thermal and solutal Grashof numbers
f_w	Suction/injection parameter
γ	Curvature parameter
$\bar{\gamma}$	Viscosity ratio (ν_{eff}/ν)
λ_T, λ_C	Thermal and solutal buoyancy parameters

Engineering quantities

Symbol	Meaning
C_f	Skin-friction coefficient
Nu_z	Local Nusselt number
Sh_z	Local Sherwood number
$f''(0)$	Dimensionless wall shear stress
$1/\theta(0)$	Dimensionless surface heat transfer rate
$-\phi'(0)$	Dimensionless surface mass transfer rate

References

[1] G. Degan, P. Vasseur, and E. Bilgen. Convective heat transfer in a vertical anisotropic porous layer. International Journal of Heat and Mass Transfer, 38(11):1975–1987, 1995.

[2] G. Degan, M. Gibigaye, C. Akowanou, and N. C. Awanou. The similarity regime for natural convection in a vertical cylindrical well filled with an anisotropic porous medium. Journal of Engineering Mathematics, 62(3):277–287, 2008.

[3] K. Vajravelu and K. V. Prasad. Mixed convection heat transfer in an anisotropic porous medium with oblique principal axes. Journal of Mechanics, 30(4):327–338, 2014.

[4] A. Nakayama, F. Kuwahara, T. Umemoto, and T. Hayashi. Heat and fluid flow within an anisotropic porous medium. Journal of Heat Transfer, 124(4):746–753, 2002.

[5] C. S. Roper, K. D. Fink, S. T. Lee, J. A. Kolodziejska, and A. J. Jacobsen. Anisotropic convective heat transfer in microlattice materials. AIChE Journal, 59(2):622–629, 2013.

[6] K. Slimi, A. Mhimid, M. Ben Salah, S. Ben Nasrallah, A. A. Mohamad, and L. Storesletten. Anisotropy effects on heat and fluid flow by unsteady natural convection and radiation in saturated porous media. Numerical Heat Transfer, Part A: Applications, 48(8):763–790, 2005.

[7] B. S. Bhadauria, A. Kumar, J. Kumar, N. C. Sacheti, and P. Chandran. Natural convection in a rotating anisotropic porous layer with internal heat generation. Transport in Porous Media, 90(2):687–705, 2011.

[8] A. M. Aly and S. E. Ahmed. An incompressible smoothed particle hydrodynamics method for natural/mixed convection in a non-Darcy anisotropic porous medium. International Journal of Heat and Mass Transfer, 77:1155–1168, 2014.

[9] M. Iasiello, N. Bianco, W. K. S. Chiu, and V. Naso. Anisotropic convective heat transfer in open-cell metal foams: Assessment and correlations. International Journal of Heat and Mass Transfer, 154:119682, 2020.

[10] S. A. Ali, M. Rudziva, and H. Sithole Mthethwa. A numerical study of doublediffusive convection in the anisotropic porous layer under rotational modulation with internal heat generation. International Communications in Heat and Mass Transfer, 137:106266, 2022.

[11] A. Garg, Y. D. Sharma, and S. K. Jain. Onset of triply diffusive thermo-bio-convection in the presence of gyrotactic microorganisms and internal heating into an anisotropic porous medium: Oscillatory convection. Chinese Journal of Physics, 84:66–82, 2023.

[12] B. Keshavarzian and H.-O. Sayehvand. Validity of the boundary layer assumptions for natural convection around a cylinder in a porous medium. Results in Engineering, 18:101069, 2023.

[13] D. A. Nield and A. Bejan. Convection in Porous Media. Springer, Cham, 5 edition, 2017.

[14] C. Y. Cheng. Double-diffusive natural convection along a vertical wavy truncated cone in non-Newtonian fluid saturated porous media with thermal and mass stratification. International Communications in Heat and Mass Transfer, 35(8):985–990, 2008.

[15] C. Y. Cheng. Combined heat and mass transfer in natural convection flow from a vertical wavy surface in a power-law fluid saturated porous medium with thermal and mass stratification. International Communications in Heat and Mass Transfer, 36(4):351–356, 2009.

[16] A. K. Kulkarni, H. R. Jacobs, and J. J. Hwang. Similarity solution for natural convection flow over an isothermal vertical wall immersed in thermally stratified medium. International Journal of Heat and Mass Transfer, 30(4):691–698, 1987.

[17] D. Angirasa and J. Srinivasan. Natural convection flows due to the combined buoyancy of heat and mass diffusion in a thermally stratified medium. Journal of Heat Transfer, 111(3):657–663, 1989.

[18] R. K. Deka and A. Paul. Convectively driven flow past an infinite moving vertical cylinder with thermal and mass stratification. Pramana, 81(4):641–665, 2013.

[19] B. K. Jha and M. K. Musa. The combined effects of anisotropic porous medium and stably stratified fluid on free convective flow through an annulus. Journal of Taibah University for Science, 12(5):678–686, 2018.

[20] B. K. Jha, M. K. Musa, and A. O. Ajibade. The role of stably stratified fluid and anisotropy porous medium in modeling fluid flow through an asymmetrically heated/cooled vertical annulus. Heat Transfer, 52(4):2972–2990, 2023.

[21] B. K. Jha, M. K. Musa, and A. O. Ajibade. Buoyancy force distribution driven Couette flow of stably stratified fluid in a vertical channel filled with anisotropic porous material. International Journal of Applied and Computational Mathematics, 9:148, 2023.

[22] J. A. Adigun, A. Adeniyan, and I. O. Abiala. Stagnation point MHD slip-flow of viscoelastic nanomaterial over a stretched inclined cylindrical surface in a porous medium with dual stratification. International Communications in Heat and Mass Transfer, 126:105479, 2021.

[23] M. Thebault, S. Giroux-Julien, V. Timchenko, C. Menezo, and J. Reizes. Transitional natural convection flow in a vertical channel: Impact of the external thermal stratification. International Journal of Heat and Mass Transfer, 151:119476, 2020.

[24] D. Srinivasacharya and Ch. RamReddy. Heat and mass transfer by natural convection in a doubly stratified non-Darcy micropolar fluid. International Communications in Heat and Mass Transfer, 37(7):873–880, 2010.

[25] M. A. Mansour, N. F. El-Anssary, and A. M. Aly. Effects of chemical reaction and thermal stratification on MHD free convective heat and mass transfer over a vertical stretching surface embedded in a porous media considering Soret and Dufour numbers. Chemical Engineering Journal, 145(2):340–345, 2008.

[26] R. Kandasamy, K. Periasamy, and K. K. S. Prabhu. Chemical reaction, heat and mass transfer on MHD flow over a vertical stretching surface with heat source and thermal stratification effects. International Journal of Heat and Mass Transfer, 48(21–22):4557–4561, 2005.

[27] F. S. Ibrahim, A. M. Elaiw, and A. A. Bakr. Effects of chemical reaction and radiation absorption on the unsteady MHD free convection flow past a semi-infinite vertical permeable moving plate with heat source and suction. Communications in Nonlinear Science and Numerical Simulation, 13(6):1056–1066, 2008.

[28] A. J. Chamkha, A. M. Aly, and M. A. Mansour. Chemical reaction effects on natural convection flow in a porous medium. Engineering Journal of Qatar University, 15:43–58, 2002.

[29] A. Mahdy. Effect of chemical reaction and heat generation or absorption on double diffusive convection from a vertical truncated cone in porous media with variable viscosity. International Communications in Heat and Mass Transfer, 37(5):548–554, 2010.

[30] P. Sudarsana Reddy and P. Sreedevi. Impact of chemical reaction and double stratification on heat and mass transfer characteristics of nanofluid flow over porous stretching sheet with thermal radiation. International Journal of Ambient Energy, 43(1):1626–1636, 2022.

[31] C. Zhang, L. Zheng, X. Zhang, and G. Chen. MHD flow and radiation heat transfer of nanofluids in porous media with variable surface heat flux and chemical reaction. Applied Mathematical Modelling, 39(1):165–181, 2015.

[32] K. Singh and P. Chauhan. Influence of heat source on radiative-convective heat and mass transfer flow of water-based copper nanofluid from a permeable stretchable cylinder in porous medium with chemical reaction and convective boundary condition. Journal of Thermal Analysis and Calorimetry, 150:1951–1968, 2025.

[33] A. J. Badday and A. J. Harfash. Double-diffusive convection in bidispersive porous medium with chemical reaction and magnetic field effects. Transport in Porous Media, 139:45–66, 2021.

[34] G. B. Zegeye, E. Haile, and G. Awgichew. Combined effects of Joule heating and binary chemical reaction of MHD Williamson nano fluid on Darcy–Forchheimer porous medium past unsteady stretching cylinder. International Journal of Thermofluids, 20:100474, 2023.

[35] H. A. Isede, A. Adeniyan, and O. Oladosu. Entropy optimization and heat transfer analysis of MHD heat generating fluid flow through an anisotropic porous parallel wall channel: An analytic solution. International Journal of Mathematical Sciences and Optimization: Theory and Applications, 9(1):81–103, July 2023.

[36] J. A. Gbadeyan, T. M. Asiru, and H. A. Isede. Influence of Dufour and Soret on unsteady, magneto-hydrodynamics (MHD), convective heat and mass transfer flow in non-Darcy porous medium. International Journal of Mathematical Sciences and Optimization: Theory and Applications, 2019(1):468–482, 2019.

[37] H. D. Nguyen, S. Paik, R. W. Douglass, and I. Pop. Unsteady non-Darcy reactiondriven flow from an anisotropic cylinder in porous media. Chemical Engineering Science, 51(22):4963–4977, 1996.

[38] A. M. Rashad. Unsteady nanofluid flow over an inclined stretching surface with convective boundary condition and anisotropic slip impact. International Journal of Heat and Technology, 35(1):82–90, 2017.

[39] L. J. Crane. Flow past a stretching plate. Zeitschrift für angewandte Mathematik und Physik ZAMP, 21(4):645–647, 1970.

[40] C. Y. Wang. Fluid flow due to a stretching cylinder. The Physics of Fluids, 31(3):466– 468, 1988.

[41] S. Znaidia, S. Rehman, N. Drissi, and F. Asiri. Mixed convection flow and heat transfer of Williamson drilling nanofluid over a stretching cylinder using Brinkman– Maxwell–Garnett model and temperature-dependent viscosity. Journal of Nonlinear Mathematical Physics, 32:18, 2025.

[42] A. Ishak, R. Nazar, and I. Pop. Uniform suction/blowing effect on flow and heat transfer due to a stretching cylinder. Applied Mathematical Modelling, 32(10):2059– 2066, 2008.

[43] N. Bachok and A. Ishak. Flow and heat transfer over a stretching cylinder with prescribed surface heat flux. Malaysian Journal of Mathematical Sciences, 4(2):159– 169, 2010.

[44] E. M. A. Elbashbeshy. Heat transfer over a stretching surface with variable surface heat flux. Journal of Physics D: Applied Physics, 31(16):1951–1956, 1998.

[45] T. S. Chen and C. F. Yuh. Combined heat and mass transfer in natural convection along a vertical cylinder. International Journal of Heat and Mass Transfer, 23(4):451– 461, 1980.

[46] I. Khan, N. Ali Shah, A. Tassaddiq, N. Mustapha, and S. A. Kechil. Natural convection heat transfer in an oscillating vertical cylinder. PLoS ONE, 13(1):e0188656, 2018.

[47] P. Virtanen, R. Gommers, T. E. Oliphant, et al. SciPy 1.0: fundamental algorithms for scientific computing in Python. Nature Methods, 17(3):261–272, 2020.